

Article

Adaptive Gaussian Mixture Model for Uncertainty Propagation Using Virtual Sample Generation

Tianlai Xu ¹, Zhe Zhang ^{2,3} and Hongwei Han ^{4,*}¹ School of Astronautics, Harbin Institute of Technology, Harbin 150001, China² Department of Mathematics and Theories, Peng Cheng Laboratory, No. 2, Xingke 1st Street, Nanshan, Shenzhen 518000, China³ Deep Space Exploration Laboratory, Beijing 100089, China⁴ School of Aerospace Engineering, Beijing Institute of Technology, Beijing 100081, China

* Correspondence: hanhongwei@bit.edu.cn

Abstract: Orbit uncertainty propagation plays an important role in the analysis of a space mission. The accuracy and computation expense are two critical essences of uncertainty propagation. Repeated evaluations of the objective model are required to improve the preciseness of prediction, especially for long-term propagation. To balance the computational complexity and accuracy, an adaptive Gaussian mixture model using virtual sample generation (AGMM-VSG) is proposed. First, an unscented transformation and Cubature rule (UT-CR) based splitting method is employed to adaptive update the weights of Gaussian components for nonlinear dynamics. The Gaussian mixture model (GMM) approximation is applied to better approximate the original probability density function. Second, instead of the pure expensive evaluations by conventional GMM methods, virtual samples are generated using a new active-sampling-based Kriging (AS-KRG) method to improve the propagation efficiency. Three cases of uncertain orbital dynamical systems are used to verify the accuracy and efficiency of the proposed manuscript. The likelihood agreement measure (LAM) criterion and the number of expense evaluations prove the performance.

Keywords: uncertainty propagation; Gaussian mixture model; adaptive splitting strategy; active sampling; virtual sample generation



Citation: Xu, T.; Zhang, Z.; Han, H. Adaptive Gaussian Mixture Model for Uncertainty Propagation Using Virtual Sample Generation. *Appl. Sci.* **2023**, *13*, 3069. <https://doi.org/10.3390/app13053069>

Academic Editor: Cristian De Santis

Received: 18 January 2023

Revised: 17 February 2023

Accepted: 20 February 2023

Published: 27 February 2023



Copyright: © 2023 by the authors. Licensee MDPI, Basel, Switzerland. This article is an open access article distributed under the terms and conditions of the Creative Commons Attribution (CC BY) license (<https://creativecommons.org/licenses/by/4.0/>).

1. Introduction

The analysis of orbit uncertainty propagation is a key step in space mission design [1,2]. Because of the existence of uncertainty, e.g., injection errors and measurement errors, the spacecraft will deviate from their nominal orbits [3,4], which may change the orbital stability and impact the performance of exploration mission [5,6]. Therefore, it is necessary to investigate the evolution of orbital uncertainty under multi-source errors [7], which provides feedback coupling inputs for control and navigation subsystem design [8,9].

Generally, uncertainty propagation is used to characterize the spacecraft's state moment (usually represented by mean and covariance matrix) or its probability density function (PDF) [10,11]. Theoretically, the uncertainty description of the orbital state can only be accurately obtained by solving Fokker-Plank Equation (FPE) [12,13] or carrying out Monte Carlo (MC) simulations [9]. Though the FPE provides accurate solutions for the propagation of the PDF, it is usually difficult to solve the equation as it is a high-dimensionally defined and nonlinear perturbed Keplerian-driven partial differential equation. The MC simulation is always considered a reliable method whose result approaches the true probability distribution when the number of MC samples tends to be infinity [14]. As a result, either FPE or MC simulations suffer from drawbacks related to a heavy computation burden [9]. To improve efficiency, some approximations are made, which can be categorized into gradient-enhanced methods and gradient-free methods [15,16].

Gradient-enhanced methods, such as state transfer matrix (STM) [17,18] and state transition tensors (STT) [19–21], analyze the orbital uncertainty by simplifying the relative nonlinear motion with the Taylor series terms [22,23]. For gradient-enhanced methods, the gradients or higher-order derivatives are incorporated for approximation [20], and analytical or semi-analytical solutions are obtained [24,25]. However, gradient-enhanced methods are only suitable for cases whose gradient information is easy to obtain. For some of the practical problems, the dynamic motion is complex, discontinuous, and nondifferentiable, and the derivatives are unavailable [16]. The gradient-free methods (also called non-intrusive methods [26]) allow for the usage of already existing orbit propagation tools as the black-box and avoid any simplifications on the fully perturbed orbital dynamics [27,28], making them conveniently extend into orbit uncertainty propagation problems [29,30]. Recently, some sample-based methods, for example, unscented transformation (UT) [31,32], Conjugate Unscented Transform (CUT) [33], and Cubature rules (CRs) [34,35], have been well investigated. These methods approximate the probability distribution at a future time by nonlinearly integrating a few sigma samples, which are deterministically chosen according to the given initial distribution [9]. The drawbacks of the above sample-based methods are that they can only deliver a second-order approximation of the distribution, which is inadequate for long-term propagation whose ultimate uncertainty distribution inevitably turns out to be highly non-Gaussian [36,37].

In order to fully characterize the non-Gaussian orbital uncertainty, the Gaussian mixture model (GMM) is commonly employed [38,39]. The basic idea of GMM is that an arbitrary PDF can be approximated, as closely as desired, by a finite sum of weighted Gaussian components (also called Gaussian PDFs). For each Gaussian component of GMM, only the mean and covariance need to be propagated because a Gaussian PDF can be completely determined with its first two moments [40,41]. Therefore, the above methods, such as QRs, UT, CUT, and CRs, can be used to propagate each Gaussian component. The GMM can better represent non-Gaussian PDFs and results in a more accurate prediction [42]. However, the GMM suffers from a heavy computation burden. Taking the CMM combined with a fifth-order CR as an example, in this case, 2190–14,600 sigma-samples are to be integrated, which is hundreds of times larger than the conventional single-Gaussian propagation using fifth-order CR [16]. Thus, it is necessary and promising to investigate approaches to enhance the efficiency of GMM.

In recent, the use of virtual sample generation (VSG) has been well discussed. The VSG is a kind of technique that aims at providing artificial samples to enlarge the current data set, which was first introduced in the field of machine learning [43,44]. Apart from the field of machine learning, the VSG technique has also been successfully applied to engineering optimization problems. Tang et al. proposed a VSG-based optimization method to reduce the required expensive evaluation [45]. Motivated by the concept of the VSG, it is possible to improve the efficiency of the GMM by incorporating virtual samples in propagation.

In this paper, an adaptive Gaussian mixture model using virtual sample generation (AGMM-VSG) is proposed. The virtual sample generation (VSG) technique [45,46] is employed to reduce the required computation for propagating each Gaussian component. Furthermore, a novel Gaussian component splitting strategy based on the virtual sample is employed for efficiently updating weights.

The paper is organized as follows. In Section 2, the orbital uncertainty propagation problem with a single Gaussian model and a GMM is described. Section 3 presents details of the proposed AGMM-VSG, followed by detailed discussions of the adaptively splitting strategy for Gaussian components and the VSG-based propagation method. The proposed AGMM-VSG is applied to three cases of uncertainty propagation for uncertain orbital dynamical systems in Section 4. Finally, Section 5 gives the conclusions.

2. Problem Statement and Methodology

2.1. Problem Statement

Consider a nonlinear dynamical system governed by the following differential equation [42]:

$$\begin{cases} \dot{x}(t) = f(x(t), t) \\ x(t_0) = x_0 \end{cases} \quad (1)$$

where $x(t) \in \mathbb{R}^n$ is the state of the system, $f(x(t), t) \in \mathbb{R}^n$ represents the sufficiently differentiable nonlinear dynamics of the system, and x_0 is the initial condition. For black-box systems, the differential equation (or gradient information) is unavailable; thus the corresponding discrete-time nonlinear system of Equation (1) is as follows:

$$\begin{cases} x(t_{k+1}) = F(x(t_k), dt_k) \\ x(t_0) = x_0 \end{cases} \quad (2)$$

In practice, it is usually assumed that the unknown uncertainties as Gaussian distribution (or Gaussian PDF), which can be represented by [10]:

$$p(x; m, P) = N(x; m, P) = \frac{1}{|2\pi P|} \exp\left\{-\frac{1}{2}(x - m)^T P^{-1}(x - m)\right\} \quad (3)$$

where $N(x; m, P)$ denotes the normal distribution with x , m and P being the input variables, mean and covariance, respectively.

2.2. Single Gaussian Model-Based Uncertainty Propagation

Generally, uncertainty propagation is used to determine the specific statistical moments of dynamics (1) or (2), with a given initial probability distribution and propagation period. The state moment, i.e., mean, and covariance matrix or probability density function (PDF) are specific quantitative measures of statistical moments. The mean and covariance matrix could be defined as follows with given random vector $x \in \mathbb{R}^n$ and PDF $p(t)$:

$$\begin{aligned} m &= E[x] = \int_{-\infty}^{\infty} \xi p(\xi) d\xi \\ P &= E[(x - m)(x - m)^T] = \int_{-\infty}^{\infty} (\xi - m)(\xi - m)^T p(\xi) d\xi \end{aligned} \quad (4)$$

where ξ is a random variable.

The Gaussian weighted integral (4) can be approximated efficiently with different quadrature rules, such as the unscented transformation (UT), Conjugate Unscented Transform (CUT), and Cubature rules (CRs). In this paper, the fifth-order CR is utilized for propagating the single Gaussian distribution. The fifth-order CR is detailed in Ref. [47], which will not be repeated here.

2.3. Gaussian Mixture Model Approach

GMM is a direct extension of the Gaussian PDF, which is given by a sum of weighted Gaussian PDFs:

$$p(x) \approx \tilde{p}(x) = \sum_{i=1}^N \alpha_i p_g(x; m_i, P_i) \quad (5)$$

where N represents the number of components of the GMM, α_i , m_i , and P_i denote the weights, mean, and the covariances associated with component i . Each Gaussian PDF $p_g(x; m_i, P_i)$ for x is defined per Equation (3). With given GMM per Equation (5), the final mean and covariance matrix is computed by:

$$\begin{aligned} m &= \sum_{i=1}^N \alpha_i m_i \\ P &= \sum_{i=1}^N \alpha_i (P_i + m_i m_i^T) - m m^T \end{aligned} \quad (6)$$

3. Methodology of Adaptive Gaussian Mixture Model Using Virtual Sample Generation

3.1. Overall Procedure of AGMM-VSG

Before introducing the methodology of the proposed AGMM-VSG, some concepts in AGMM-VSG are explained as follows:

Definition 1. (point, response, and sample): As is shown in Table 1, the point is a kind of pure coordinate. In AGMM-VSG, point refers to any vector of state $\mathbf{x}(t_k)$ at time t_k . The response is taken as the output of the black-box model (2), i.e., the state vector $\mathbf{x}(t_{k+1})$, which corresponds to the point $\mathbf{x}(t_k)$. A sample is a combination of a point and its response.

Table 1. Description of point, response and sample.

Item	Symbol	Description	Other Statement
Point	$\mathbf{x}(t_k)$	Input of the black-box model	Pure coordinate
Response	$\mathbf{x}(t_{k+1})$	Output of the black-box model	-
Sample	$(\mathbf{x}(t_k), \mathbf{x}(t_{k+1}))$	Combination of a point and its response	-

Definition 2. (real sample and virtual sample): The real sample represents a combination of a point and its real response generated by invoking expensive black-box simulations while the virtual sample refers to the combination of a point and its virtual response generated without calling expensive simulations. The virtual responses are only generated using the active KRG model. Note that the number of real samples indicates the computational expense of the uncertainty propagation. Moreover, in this paper, the virtual response is generated by the active sampling-based KRG model, and the expense to generate virtual samples is negligible.

Definition 3. (cheap point and superior cheap point): Cheap point is a point generated according to the given PDF. Note that the actual response of a cheap point is not calculated, and therefore, the computational cost is negligible. The cheap points are drawn as a candidate pool for constructing the AS-KRG model. The superior cheap point has a promising performance for improving the global accuracy of the KRG model, which is classified on basis of the variance predicted using the KRG model. The process of using both the cheap point and superior cheap point will be detailed in Section 3.3.

The flowchart of AGMM-VSG is shown in Figure 1, and the procedure is explained in detail as follows:

Step 1: The parameters of the problem are determined, including the black-box discrete dynamics, the initial PDF (or initial mean and covariance matrix), the propagating period t_f , and discrete-time dt . Other necessary items, such as the maximal number of samples for constructing the KRG model and splitting library, will be discussed in the next section. The current time epoch is set to be zero, i.e., $t = 0$.

Step 2: In the first iteration, the single Gaussian model is used, with its mean and covariance matrix equaling the initial PDF. The number of Gaussian mixture components is one.

Step 3: The KRG model is first constructed using initial real samples and then is gradually refined with newly added real samples. The constructed KRG model is utilized for generating virtual samples.

Step 4: Propagate each component using fifth-order CR. Note that only virtual samples are used when propagating; thus, the expense of this step is negligible. Renew the current time epoch, i.e., $t = t + dt$.

Step 5: For each component, determine whether the splitting process should be executed. If it should, then apply a univariate splitting library in a specified direction, i.e., the principal (eigenvector) direction of the covariance matrix.

Step 6: If $t < t_f$, jumps to Step 3. Otherwise, it outputs the results.

The algorithms of Gaussian components splitting and virtual sample generation-based propagation are detailed in Sections 3.2 and 3.3, respectively.

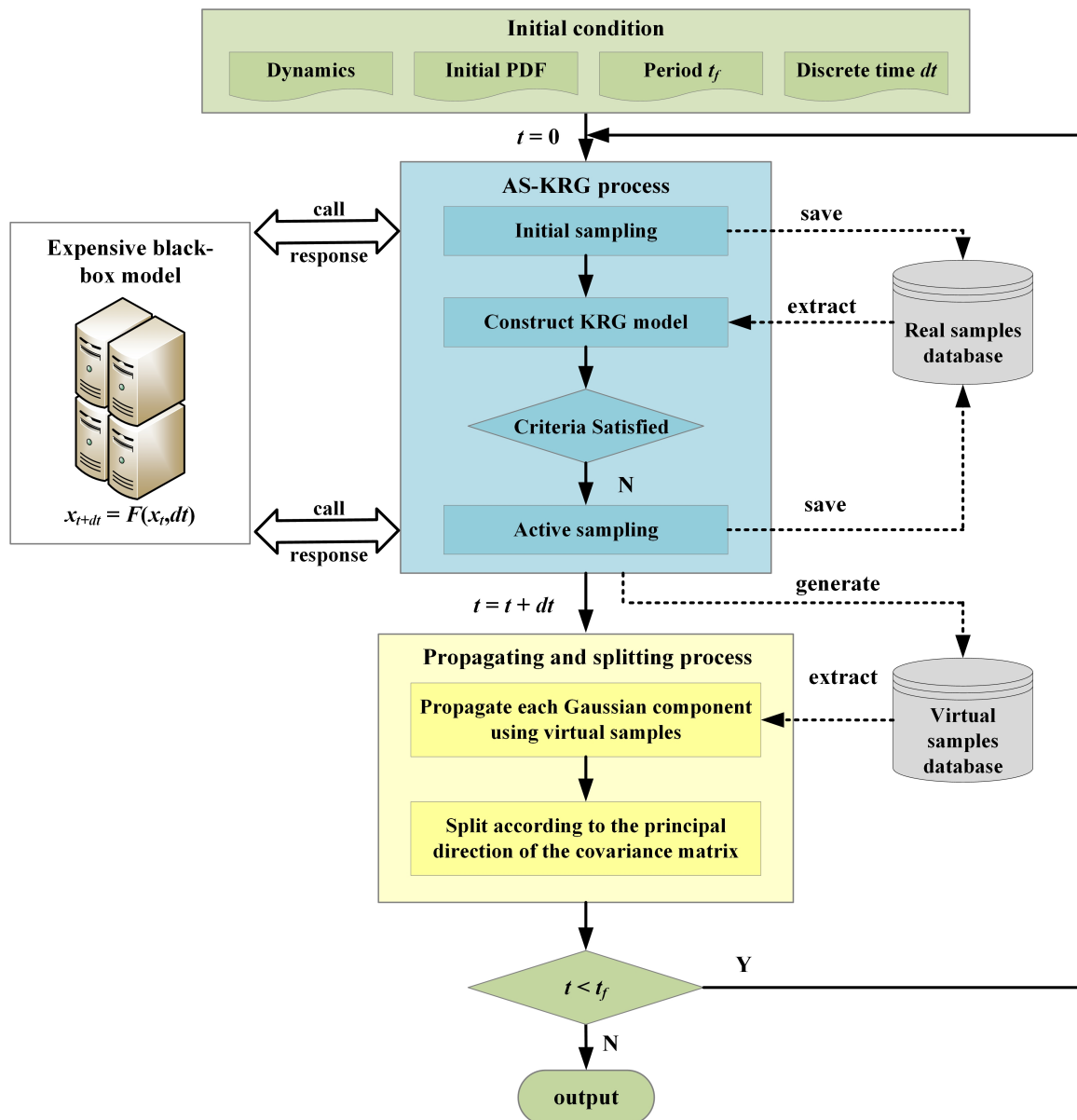


Figure 1. Flowchart of AGMM-VGS.

3.2. Gaussian Component Nonlinearity Detecting

It is noted that only the linear propagation can maintain the Gaussian property, and any deviation in the nonlinear dynamics from the linearized solution may indicate nonlinear effects. This deviation can be handled by specifying a threshold and monitoring the nonlinearity [48]. That is to say, when the nonlinearity causes a more significant non-Gaussian property, a component of the GMM can be split into finer Gaussian components. A split GMM component is considered “finer” because Gaussians with smaller covariances would remain more Gaussian compared with ones with larger covariances, which will make the uncertainty propagation more representative. Thus, an adaptive GMM with splitting technologies is necessary, especially for long-term propagation. In this section, a novel unscented transformation and Cubature rule-based (UT-CR) method for monitoring (or detecting) the nonlinearity is introduced, and the Gaussian component splitting will be detailed in the next section.

Usually, the term entropy is used for detecting nonlinearity [42]. For a Gaussian distribution with the determinant of a scaled form of the covariance matrix, the corresponding differential entropy (DE), in terms of the logarithm, is given as:

$$H(\mathbf{x}) = \frac{1}{2} \log |2\pi e \mathbf{P}| \quad (7)$$

where the temporal derivative of the DE is given by:

$$\dot{H}(\mathbf{x}) = \frac{1}{2} \text{trace} \{ \mathbf{P}^{-1} \dot{\mathbf{P}} \} \quad (8)$$

where $\dot{\mathbf{P}}$ is the temporal derivative of the covariance matrix \mathbf{P} .

In case of a linearized representation, the time rate of the DE is written as:

$$\dot{H}(\mathbf{x}) = \frac{1}{2} \text{trace} \{ \mathbf{f}_x \} \quad (9)$$

where $\mathbf{f}_x = \partial \mathbf{f} / \partial \mathbf{x}$ represents the linearized dynamics Jacobian.

It is worth noting that for linearized dynamics, $\dot{H}(\mathbf{x}) = 0$, meaning that the differential entropy is constant for the linearized system, making the DE unable to be used for splitting the Gaussian components for the linearized system. In this paper, a UT-CR-based splitting strategy is utilized to detect nonlinearity.

The novel dynamic nonlinearity index measures the departure from linearity as [49]:

$$v(t, t_0) = \frac{\| \Phi_{CR5}(t, t_0) - \Phi_{UT}(t, t_0) \|}{\| \Phi_{UT}(t, t_0) \|} \quad (10)$$

where $v(t, t_0)$ is the dynamic nonlinearity index and $\| \cdot \|$ represents the norm. The $\Phi_{CR5}(t, t_0)$ and $\Phi_{UT}(t, t_0)$ are the STM obtained by fifth-order CR (CR5) and UT, respectively. It is noted that the UT could capture the solutions accurately to the third order while the CR5 could capture accurately to the fifth order; thus, the nonlinearity with fourth and fifth orders are introduced with the index $v(t, t_0)$.

The STM $\Phi_{CR5}(t, t_0)$ and $\Phi_{UT}(t, t_0)$ are obtained as follows. First, the posterior covariances (transformed distribution) $\mathbf{P}_{CR5}(t, t_0)$ and $\mathbf{P}_{UT}(t, t_0)$ are calculated using fifth-order CR and UT, given the same prior probability $\mathbf{P}(t_0) = \mathbf{P}_0$. Consider the following first-order approximation of the covariance of the transformed distribution [50]:

$$\begin{aligned} \mathbf{P}_{CR5}(t) &= \Phi_{CR5}(t, t_0) \mathbf{P}_0 \Phi_{CR5}^T(t, t_0) \\ \mathbf{P}_{UT}(t) &= \Phi_{UT}(t, t_0) \mathbf{P}_0 \Phi_{UT}^T(t, t_0) \end{aligned} \quad (11)$$

If the Cholesky factorization $\mathbf{P}_0 = \mathbf{L}_0 \mathbf{L}_0^T$, $\mathbf{P}_{CR5}(t) = \mathbf{L}_{CR5}(t) \mathbf{L}_{CR5}^T(t)$ and $\mathbf{P}_{UT}(t) = \mathbf{L}_{UT}(t) \mathbf{L}_{UT}^T(t)$, where \mathbf{L}_0 , $\mathbf{L}_{CR5}(t)$ and $\mathbf{L}_{UT}(t)$ are the corresponding unique lower triangular “square root” matrixes. Therefore, Equation (11) is rewritten as:

$$\begin{aligned} \mathbf{L}_{CR5}(t) \mathbf{L}_{CR5}^T(t) &= \Phi_{CR5}(t, t_0) \mathbf{L}_0 \mathbf{L}_0^T \Phi_{CR5}^T(t, t_0) \\ \mathbf{L}_{UT}(t) \mathbf{L}_{UT}^T(t) &= \Phi_{UT}(t, t_0) \mathbf{L}_0 \mathbf{L}_0^T \Phi_{UT}^T(t, t_0) \end{aligned} \quad (12)$$

A transformation equation can be written as:

$$\begin{aligned} \mathbf{L}_{CR5}(t) &= \Phi_{CR5}(t, t_0) \mathbf{L}_0 \\ \mathbf{L}_{UT}(t) &= \Phi_{UT}(t, t_0) \mathbf{L}_0 \end{aligned} \quad (13)$$

The solution for Equation (13) is as:

$$\begin{aligned} \Phi_{CR5}(t, t_0) &= \mathbf{L}_{CR5}(t) \mathbf{L}_0^{-1} \\ \Phi_{UT}(t, t_0) &= \mathbf{L}_{UT}(t) \mathbf{L}_0^{-1} \end{aligned} \quad (14)$$

Substitute Equation (14) into Equation (10), we arrive at the following expression of dynamic nonlinearity index:

$$\begin{aligned} v(t, t_0) &= \frac{\|L_{CR5}(t)L_0^{-1} - L_{UT}(t)L_0^{-1}\|}{\|L_{UT}(t)L_0^{-1}\|} = \frac{\|(L_{CR5}(t) - L_{UT}(t))L_0^{-1}\|}{\|L_{UT}(t)L_0^{-1}\|} \\ &= \frac{\|L_{CR5}(t) - L_{UT}(t)\|/\|L_0\|}{\|L_{UT}(t)\|/\|L_0\|} = \frac{\|L_{CR5}(t) - L_{UT}(t)\|}{\|L_{UT}(t)\|} \end{aligned} \quad (15)$$

The fewer the values the nonlinearity index indicates, the less significant the nonlinearity. Note that the virtual samples, which will be discussed in the next subsection, can be used for propagating the $P_{CR5}(t)$ and $P_{UT}(t)$ to reduce computation cost.

3.3. Gaussian Component Splitting

Once the nonlinearity is detected, then the splitting is to be executed. Current splitting algorithms can be summarized into two categories: (1) Split a Gaussian PDF in all directions or (2) Split a Gaussian PDF by applying a univariate splitting library in a specified direction [48]. Solving an L2-minimization optimization problem is usually required when using the first kind of method, which incurs additional computational consumption. In this paper, splitting in one direction is employed. The multivariate Gaussian PDF is split by applying a univariate splitting library in the direction of maximum eigenvalue, which is given per the following steps:

First a standard normal distribution $p(x; 0, 1)$ is split into N' homoscedastic Gaussian distributed components as $N'p(x; 0, 1) \approx \sum_{i=1}^{N'} \tilde{\alpha}_i p_g(x; \tilde{m}_i, \tilde{\sigma}_i^2)$. This step is independent from the concerned problem; therefore, parameters $(\tilde{\alpha}_i, \tilde{m}_i, \tilde{\sigma}_i)$ can be computed offline and saved as a splitting library. The computation of the splitting parameters is well-provided by [42], and one case with is illustrated in Table 2.

Table 2. Five-component splitting library with $\beta = 2$ and $\lambda = 0.0025$ [42].

Component i	α_i	\tilde{m}_i	$\tilde{\sigma}_i$
1	0.0763216491	−1.6899729111	0.4422555386
2	0.2474417860	−0.8009283834	0.4422555386
3	0.3524731300	0	0.4422555386
4	0.2474417860	0.8009283834	0.4422555386
5	0.0763216491	1.6899729111	0.4422555386

Then, consider the spectral factorization of the covariance matrix P_i as:

$$P_i = V\Lambda_i V^T \quad (16)$$

where $\Lambda_i = \text{diag}\{[\lambda_1, \dots, \lambda_k, \dots, \lambda_n]\}$ is the eigenvalues matrix with λ_k being the k -th largest eigenvalue of the covariance matrix P_i . The i -th component is approximated by $p_g(x; m_i, P_i) \approx \sum_{j=1}^{N'} \tilde{\alpha}_j p_{g,j}(x; m_{i,j}, P_{i,j})$ with mean and covariance matrix given as:

$$m_{i,j} = m_i + \sqrt{\lambda_k} \tilde{m}_j v_k \quad (17)$$

$$P_{i,j} = V\tilde{\Lambda}_i V^T \quad (18)$$

where v_k is the k -th eigenvector of P_i and $\tilde{\Lambda}_i = \text{diag}\{[\lambda_1, \dots, \lambda_k, \dots, \lambda_n]\}$ is the set of eigenvalues of the i -th new component.

3.4. Virtual Sample Generation-Based Propagation Strategy

It is noted that for a black-box model, only sample-based gradient-free methods can be used for single Gaussian component propagation, and fifth-order CR is selected in this paper, as is shown in Equation (19).

$$\lambda \int_{\infty} F(x)p(x; \mathbf{m}, \mathbf{P})dx = \int_{\infty} F(\mathbf{A}\mathbf{x} + \mathbf{m})p(x; \mathbf{m}, \mathbf{P})dx \approx \sum_{i=1}^{N_p} W_i F(\gamma_i) \quad (19)$$

where $\gamma_i (i = 1, \dots, N_p)$ are Cubature points according to the fifth-order CR.

Although the Gaussian component splitting technology could reduce unnecessary components, the computation burden, if real samples are involved when propagating, is still intractable. However, the computation burden can be released by using virtual samples with the information hidden in the raw samples (some already obtained real samples):

$$\int_{\infty} F(x)p(x; \mathbf{m}, \mathbf{P})dx \approx \sum_{i=1}^{N_p} W_i F(\gamma_i) \approx \sum_{i=1}^{N_p} W_i \tilde{F}(\gamma_i) \quad (20)$$

where $\tilde{F}(\gamma_i)$ is the response of the virtual samples.

Generally, virtual samples can be constructed using prior knowledge, the addition of noise, and existing datasets. In this paper, an active sampling-based KRG model based on existing datasets is proposed for generating virtual samples for the black-box uncertainty model.

KRG [16,51] is an interpolation metamodeling technique as shown in Equation (20).

$$f_{KRG}(\mathbf{x}) = G(\mathbf{x}) + Z(\mathbf{x}) \quad (21)$$

where $f_{KRG}(\mathbf{x})$ is the output function of the KRG model, $G(\mathbf{x})$ captures the major trend of input–output mapping, and $Z(\mathbf{x})$ is a zero-mean, unit-variance stationary Gaussian process that determines the approximation ability of the KRG model. The covariance matrix of $Z(\mathbf{x})$ is given as follows:

$$\text{Cov}(Z(\mathbf{x}_i), Z(\mathbf{x}_j)) = \sigma^2 R[R(\mathbf{x}_i, \mathbf{x}_j)] \quad (22)$$

where σ^2 is the process variance of $Z(\mathbf{x})$, R is the correlation matrix, and $R(\cdot, \cdot)$ is a Gaussian correlation function that controls the smoothness of the KRG model. Note that in addition to the output predicted using the KRG model, the variance, which can be taken as the degree of confidence of the prediction, can also be obtained.

The performance of the KRG model will influence the accuracy of the virtual samples, which, in turn, will influence the accuracy of propagation. Although investigations have been conducted to improve the global accuracy of the KRG model, it is still difficult to use a static metamodel to accurately approximate a sophisticated problem (e.g., high-dimensional nonlinear problem) with sparsely scattered samples. However, to improve the convergence and efficiency, the adaptive sampling is actually realized by the management of the online KRG models [46]. In this paper, an adaptive sampling called the “active sampling method” is adopted, with which the superior cheap points are adaptively selected.

The least-confidence strategy is adopted in this paper to perform the active sampling. The superior sample is selected according to the following metric:

$$\mathbf{x}^* = \arg \max Var_{RBF}(\mathbf{x}) \quad (23)$$

where $Var_{RBF}(\mathbf{x})$ is the variance of the output prediction $f_{KRG}(\mathbf{x})$. Comparison studies in Ref. [46] have proven that the KRG generally has better approximation accuracy than other technologies, for example, RBF and Gaussian Process (GP) [52], in the condition of relatively sparse samples and lack of prior knowledge. In contrast, the construction expense of KRG is more expensive than that of the Radial basis function (RBF) [53]. Therefore, to

further reduce the expense, in this paper, up to n_{add} samples, with the larger variances, are added into the sample set at each iteration, for constructing the KRG model, where n_{add} is the user-defined parameter. In this paper, the KRG model is constructed using MATLAB toolbox SURROGATES.

The procedure of this strategy is exhibited in detail as follows:

Step 1: The parameters are determined, including the total number of cheap points n_c , the number of superior cheap points added at each iteration n_{add} , the maximal number of real samples n_r , and the number of initial real samples n_i .

Step 2: Generate n_c points according to the current PDF $p(x, t)$ as the candidate points set; denote as $S_c^0 = \{x_1, x_2, \dots, x_{n_c}\}$. Select n_i points from the candidate points set S_c^0 , note as $S_s = \{x_{i_1}, x_{i_2}, \dots, x_{i_{n_i}}\}$. Evaluate the points in S_s using black-box dynamical model (2), and then responses are obtained. All of these n_i points and their corresponding responses make up the sample set. Construct an RBF model based on the existing samples. Renew the candidate points set as $S_c^1 = \{x \mid x \in S_c^0 \text{ and } x \notin S_s\}$. The iteration counter k is set to be one, i.e., $k \leftarrow 1$. The current number of real samples n_s is set to be $n_s = n_i$.

Step 3: Evaluate all the points in candidate points set S_c^k using the KRG model. Sort these points according to their predicted variances. The top n_{add} superior points are selected, noted as S_{add}^k . Evaluate these points and then add them to the sample set. Construct the RBF model. Remove the selected superior points from the candidate points set as $S_c^{k+1} = \{x \mid x \in S_c^k \text{ and } x \notin S_{add}^k\}$, $k \leftarrow k + 1$, $n_s \leftarrow n_s + n_{add}$.

Step 4: If $n_s < n_r$, return to *Step 3*; otherwise jump to *Step 5*.

Step 5: Use the virtual sample evaluated by the KRG model to propagate.

To further demonstrate the process of active sampling based KRG model, a one-dimensional numerical benchmark is tested. The benchmark describes the mapping relation between the final position error along the x -axis and the initial velocity error along the y -axis, which is given as:

$$g(\Delta v_y(t_0)) = \Delta r_x(t_f) \quad (24)$$

The spacecraft moves on the equatorial plane and the dynamics considered the Earth's gravity and atmospheric drag, which is governed by [42]:

$$\begin{aligned} \mathbf{x} &= [\mathbf{r}^T, \mathbf{v}^T]^T = [r_x, r_y, v_x, v_y]^T \\ \dot{\mathbf{x}} &= \mathbf{f}(\mathbf{x}) = [v_x, v_y, -\mu r_x r^{-3} - \rho(h)\beta v_{rel} v_{rel,x}/2, -\mu r_y r^{-3} - \rho(h)\beta v_{rel} v_{rel,y}/2]^T \end{aligned} \quad (25)$$

where $r = \sqrt{r_x^2 + r_y^2}$, $v_{rel,x} = v_x - \omega r_y$, $v_{rel,y} = v_y - \omega r_x$, and ω is the angular velocity of the Earth. $\rho(h)$ is the atmospheric density as a function of the altitude of the object. Additionally, it is assumed that the atmospheric density is described by an exponential atmosphere model via:

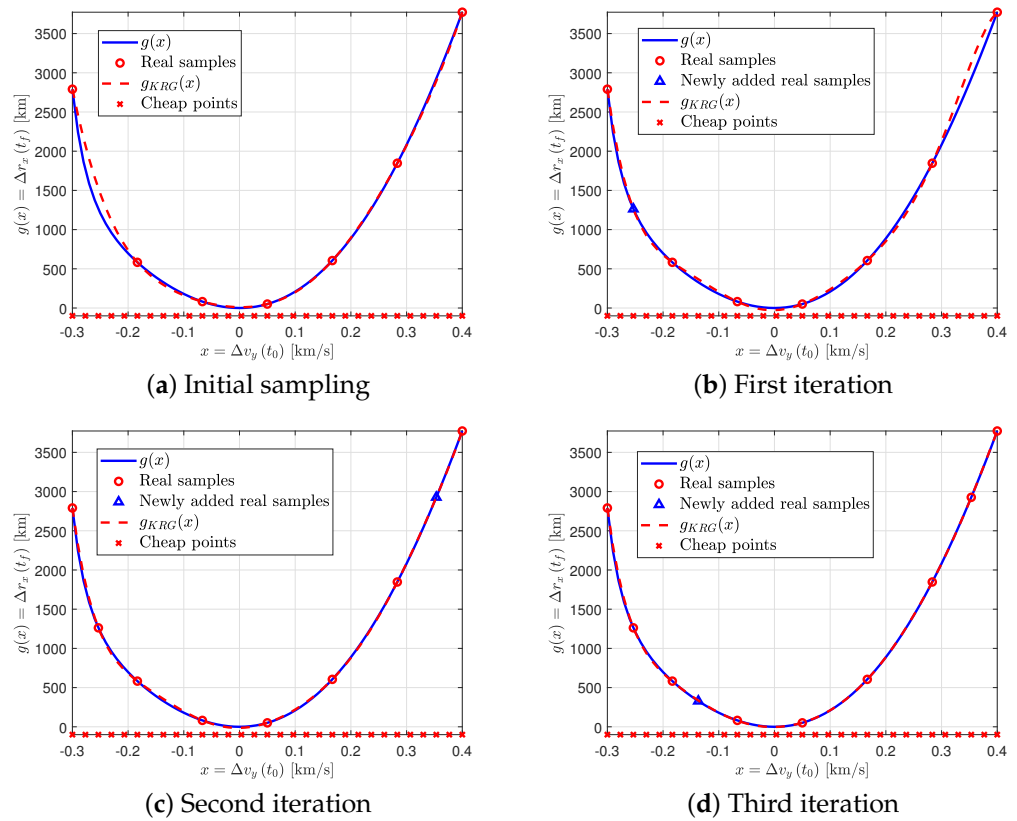
$$\rho(h) = \rho_0 \exp\{-(h - h_0)/h_s\} \quad (26)$$

with $\rho_0 = 3.614 \times 10^{-13}$ kg/m³, $h_0 = 700$ km and $h_s = 88.667$ km. β is the ballistic coefficient of the object, and it is taken to be 1.4 in this paper.

The elements of the nominal orbit are illustrated in Table 3, and the propagation time is set to be one nominal orbit period, which is about 5331.288 s. The points are set to be evenly distributed in range. The cheap points, real samples, and newly added real samples (superior cheap points) are illustrated in Figure 2. As is shown in Figure 2, the newly added real samples (blue triangle) are selected where the KRG model is the most unconfident. Note that the global accuracy of the KRG model is improved when samples are added sequentially.

Table 3. Elements of the nominal orbit of LEO case.

a/km	e	i/deg	Ω/deg	ω/deg	n/deg
6596	0	0	0	0	0

**Figure 2.** Active sampling for one-dimensional numerical benchmark.

4. Numerical Simulations

In this section, the developed AGMM-VSG method for uncertainty propagation is applied to the propagation of uncertainty for two test problems, i.e., a high-Earth orbit case and a low-Earth orbit case. The performance of the proposed AGMM-VSG method is discussed by comparing it with the conventional fifth-order Cubature rule and adaptive Gaussian mixture model method.

4.1. High-Earth Orbit Case

First, consider a spacecraft orbiting on a high-Earth orbit (HEO). Assume that the motion of the spacecraft is confined to the equatorial plane, which allows the position r to be described by two scalar values r_x and r_y , and the velocity v to be described by two scalar values v_x and v_y . Thus, the state vector and equations of motion that describe the nonlinear dynamical system are written as follows [42]:

$$\begin{aligned} \mathbf{x} &= [\mathbf{r}^T, \mathbf{v}^T]^T = [r_x, r_y, v_x, v_y]^T \\ \dot{\mathbf{x}} &= \mathbf{f}(\mathbf{x}) = [v_x, v_y, -\mu r_x r^{-3}, -\mu r_y r^{-3}]^T \end{aligned} \quad (27)$$

where $\mu = 398,600$ is the gravitational constant of the central body (i.e., Earth in this paper).

Take notice that although dynamics (27) are of the analytical form, it is still considered a black-box model by invoking the kinetic integral $F(t) = \int_0^t \mathbf{f}(\mathbf{x}) d\mathbf{x}$.

The elements of the nominal orbit are listed in Table 4, given by a semimajor axis of 35,000 km and an eccentricity of 0.2.

Table 4. Elements of the nominal orbit of HEO case.

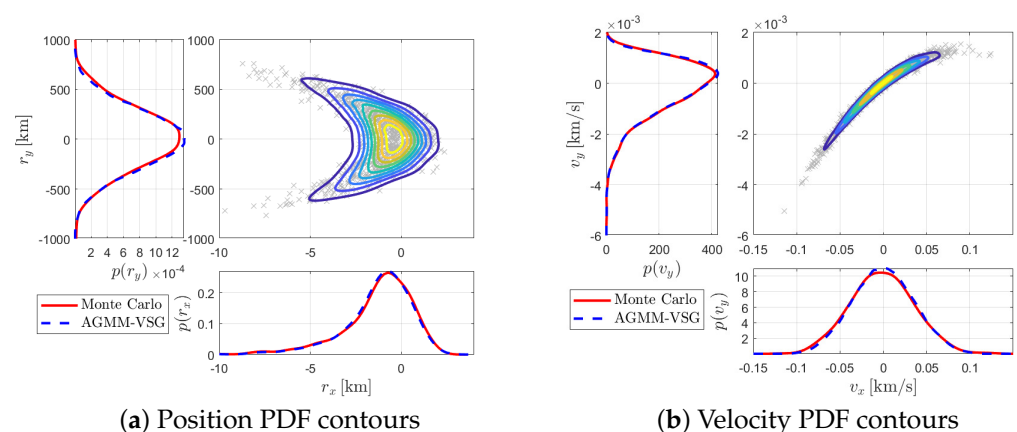
a/km	e	i/deg	Ω/deg	ω/deg	n/deg
35,000	0.2	0	0	0	0

The initial state distribution is taken to be Gaussian, with the initial mean represented by the nominal orbit elements. Additionally, the initial covariance is set to be diagonal with standard deviations in the position elements of 1 km and the velocity elements of 1 m/s:

$$P_0 = \text{diag}\left([1 \text{ km}^2, 1 \text{ km}^2, 10^{-6} \text{ km}^2/\text{s}^2, 10^{-6} \text{ km}^2/\text{s}^2]\right) \quad (28)$$

To characterize the performance of the proposed AGMM-VSG method, both the AGMM-VSG and fifth-order CR methods are applied to the problem of predicting the evolution of uncertainty. The propagation time is one orbit period (around 65,164.833 s). The values of parameters to be used in AGMM-VSG are set as $t_f = 65,164.833 \text{ s}$, $dt = t_f/100$. The criterion for splitting the Gaussian components are $v > 10^{-4}$, where v is the nonlinearity index (Equation (15)) of the corresponding component. Parameters for active sampling are given as: $n_c = 200$, $n_r = 100$, $n_i = 50$, and $n_{add} = 10$.

In addition, a Monte Carlo simulation using 1000 samples drawn from the initial distribution is performed. The position and velocity marginal PDF contours using AGMM-VSG and fifth-order CR are illustrated in Figures 3 and 4, respectively. The outputs of the Monte Carlo simulations are shown represented with a grey x. Depart from the scatter plot, the PDFs of each state variable are also illustrated. The PDFs of each state variable of AGMM-VSG and fifth-order CR are obtained by calculating the integral of the multivariate PDFs, while PDFs of each state variable of 1000 Monte Carlo samples are obtained using MATLAB function *ksdensity*. It can be seen from Figures 3 and 4 that, compared with fifth-order CR, the proposed method is better at representing the curvature exhibited by the Monte Carlo samples. For AGMM-VSG, only 65 Gaussian components and 100 real samples are requested. The computation cost of AGMM-VSG is a little higher than that of fifth-order CR, which uses a total of 33 evaluations ($2n^2 + 1$ Cubature-points and $n = 4$), while significantly outperforming fifth-order CR in terms of accuracy. Moreover, if use real samples for propagating, a total of 2145 real samples (65 components and 33 evaluations for each component) are needed, which indicates the signification of the utilization of virtual samples for reducing computational expense.

**Figure 3.** PDF contours using AGMM-VSG with Monte Carlo samples of HEO case.

To further provide a relative comparison of the performance of the two solutions obtained (from the AGMM-VSG and fifth-order CR), a criterion called the likelihood agreement measure (LAM) is utilized [42]. The LAM is used to evaluate the likelihood

agreement between two distributions. Given two PDFs, noted as $p(x)$ and $q(x)$, the LAM is defined as:

$$\text{LAM}(p, q) = \int_{-\infty}^{\infty} p(x)q(x)dx \quad (29)$$

where Equation (29) represents the density of overlap between the two PDFs. The greater agreement for one PDF with another PDF, the larger their densities.

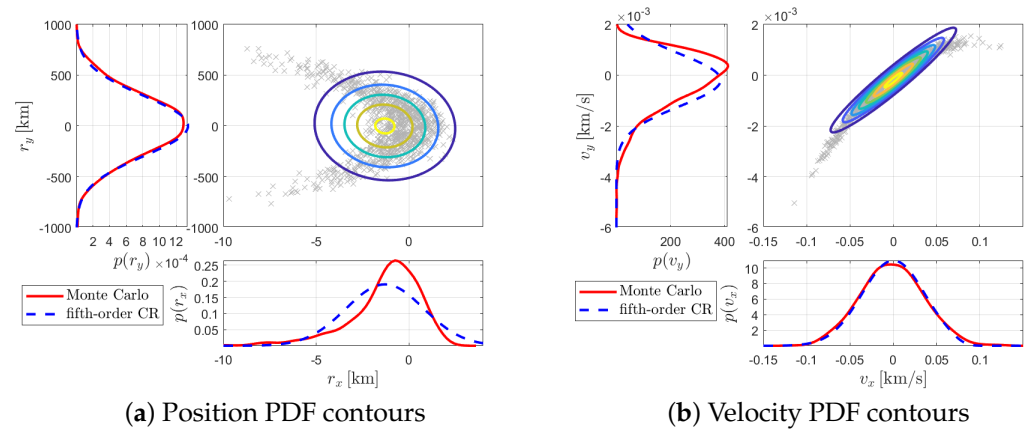


Figure 4. PDF contours using fifth-order CR with Monte Carlo samples of HEO case.

However, the analytical distribution is intractable to obtain. In a practical problem, the true distribution is approximated using the Monte Carlo samples, and the LAM is rewritten as

$$\text{LAM}(p, q) = \sum_{i=1}^N \sum_{j=1}^O \alpha_i \gamma_j p_g(x_j; m_i, P_i) \quad (30)$$

where Q is the total number of samples within the Monte Carlo simulation.

The accuracy of different methods can be compared using the same set of Monte Carlo samples. The LAM of the proposed AGMM-VSG and fifth-order CR are drawn in Figure 5. Moreover, the LAM of the AGMM method, where only real samples are employed, is also tested as the standard results. To be clear, the likelihood measure of the AGMM-VSG is normalized by the value for the AGMM method. It can be observed that the LAM of AGMM-VSG is close to that of AGMM, while clearly outperforming the fifth-order CR method.

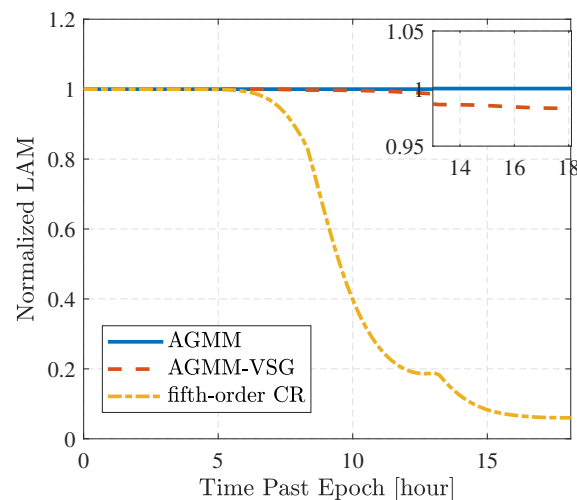


Figure 5. Likelihood agreement measure for the AGMM, AGMM-VSG, and fifth-order CR of HEO case.

4.2. Low-Earth Orbit Case

The dynamic system for the low-Earth-orbit propagation is given per Equation (25). The elements of the nominal orbit are illustrated in Table 3, and the propagation time is set to be one nominal orbit period. The initial covariance is taken to be diagonal with standard deviations of 1.3 km in position r_x , 0.5 km in position r_y , 2.5 m/s in velocity v_x , and 5 m/s in velocity v_y , that is:

$$P_0 = \text{diag}\left(\left[0.5^2 \text{ km}^2, 2.5^2 \text{ km}^2, 2.5^2 \times 10^{-6} \text{ km}^2/\text{s}^2, 5^2 \times 10^{-6} \text{ km}^2/\text{s}^2\right]\right) \quad (31)$$

Similarly to the previous example, the performance of AGMM-VSG is verified by comparing it with fifth-order CR. The parameters involved in AGMM-VSG are set to be the same as the previous HEO case, and the results are shown in Figures 6 and 7. From Figures 6 and 7, it is seen that both implementations of the AGMM-VSG approach enable a better representation of the curvature exhibited by the Monte Carlo samples.

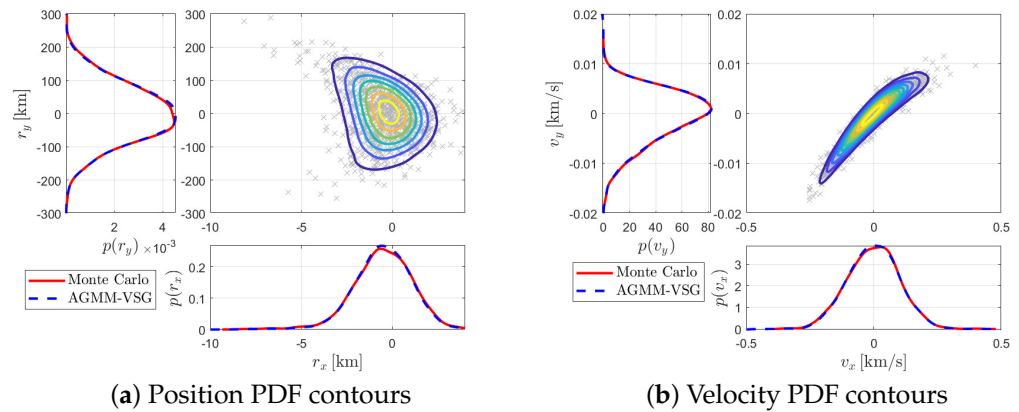


Figure 6. PDF contours using AGMM-VSG with Monte Carlo samples of LEO case.

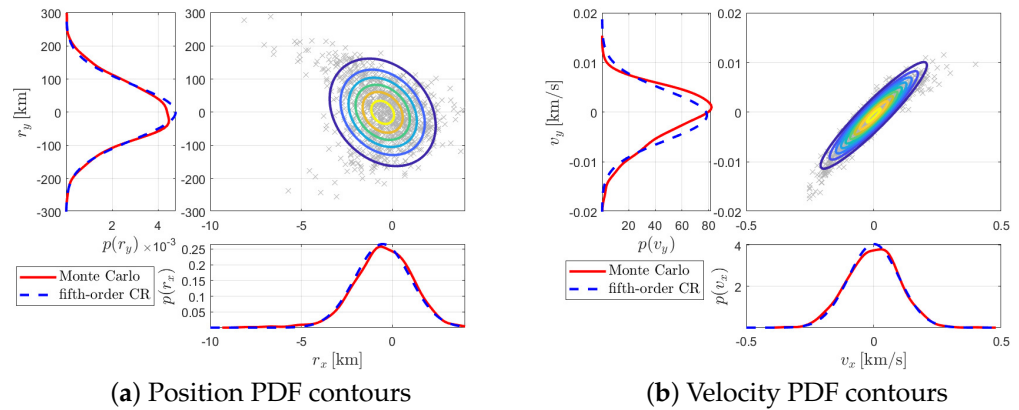


Figure 7. PDF contours using fifth-order CR with Monte Carlo samples of LEO case.

Additionally, 25 components are used to represent the final PDF, and only 100 evaluations are requested. The LAMs of AGMM, AGMM-VSG, and fifth-order CR are also normalized to provide a clear relative measure. The results are illustrated in Figure 8. It is easy to observe that the fifth-order CR is outperformed by both AGMM and AGMM-VSG.

With the validation of the two numerical simulations validation, the advantages of the AGMM-VSG method in accuracy and efficiency can be recapitulated. The proposed AGMM-VSG could represent the distribution as well as AGMM, and is better than the fifth-order CR method, while it is much more efficient than the AGMM.

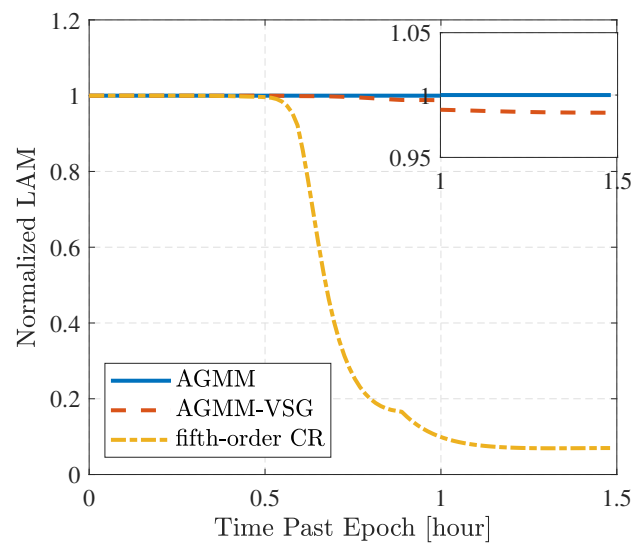


Figure 8. Likelihood agreement measure for the AGMM, AGMM-VSG, and fifth-order CR of LEO case.

4.3. TianQin Orbit Uncertainty Propagation

To demonstrate the effectiveness and practicality of the proposed AGMM-VSG in solving uncertainty propagation of computationally expensive, black-box systems, as well as the application in real-world space-based GW observatories, a case of TianQin Orbit (TQO) is investigated.

The state of the detector is defined as $x = [r_x, r_y, r_z, v_x, v_y, v_z]^T$. The high-fidelity dynamics model includes an 8×8 spherical-harmonic Earth gravity field (JGM-3), the point-mass gravity field from the Moon, and the Sun (the ephemeris JPL405). The spacecraft of TianQin each have a disturbance reduction system (DRS) needed to reduce the effects of the non-gravitational forces [54]; thus, the solar radiation pressure and the atmospheric drag are neglected.

The elements of the nominal orbit of one detector of TianQin are shown in Table 5. The orbit is propagated in one period, which is about 314,710.3177 s.

Table 5. Elements of the nominal orbit of TQO case.

a/km	e	i/deg	Ω/deg	ω/deg	n/deg
99,995.572323	0.000430	94.697997	210.445892	358.624463	61.329603

Both the AGMM-VSG and the fifth-order CR are applied to the above TQO problem of predicting the evolution of uncertainty. In employing the AGMM-VSG, the criterion for splitting the Gaussian components is set to be $v > 10^{-3}$, and the number of evaluations for constructing the surrogates in each iteration is set to 300. The final state uncertainty and their corresponding means and 3σ ellipsoids, using proposed AGMM-VSG and MC, are projected in Figure 9. It is witnessed that the accuracy of AGMM-VSG and MC are almost the same when considering the first two moments. Moreover, the projection of the predicted PDF from the AGMM-VSG, together with the 1000 Monte Carlo samples, are shown in Figure 10. It is clearly observed that both the implementations of the position and velocity of the AGMM-VSG approach characterize the non-linearity of the MC samples-approximated distribution.

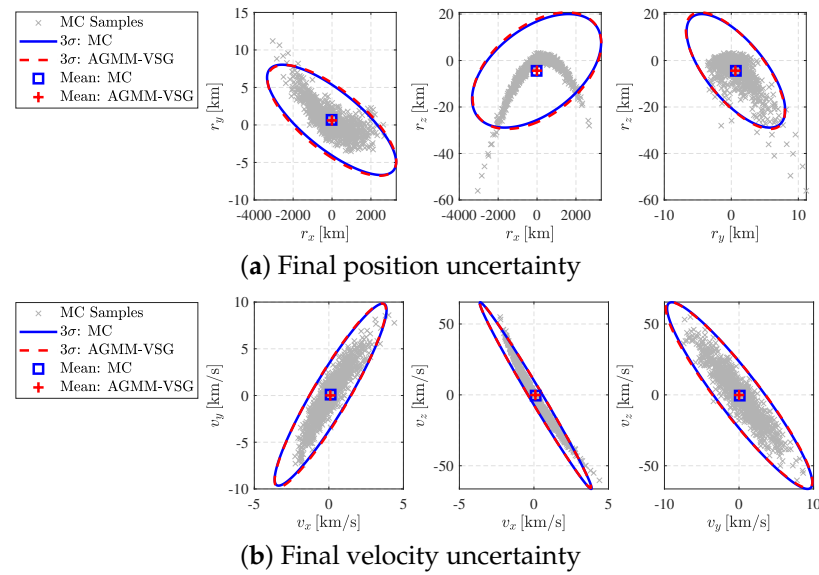


Figure 9. Final uncertainty using AGMM-VSG and MC for TQO case.

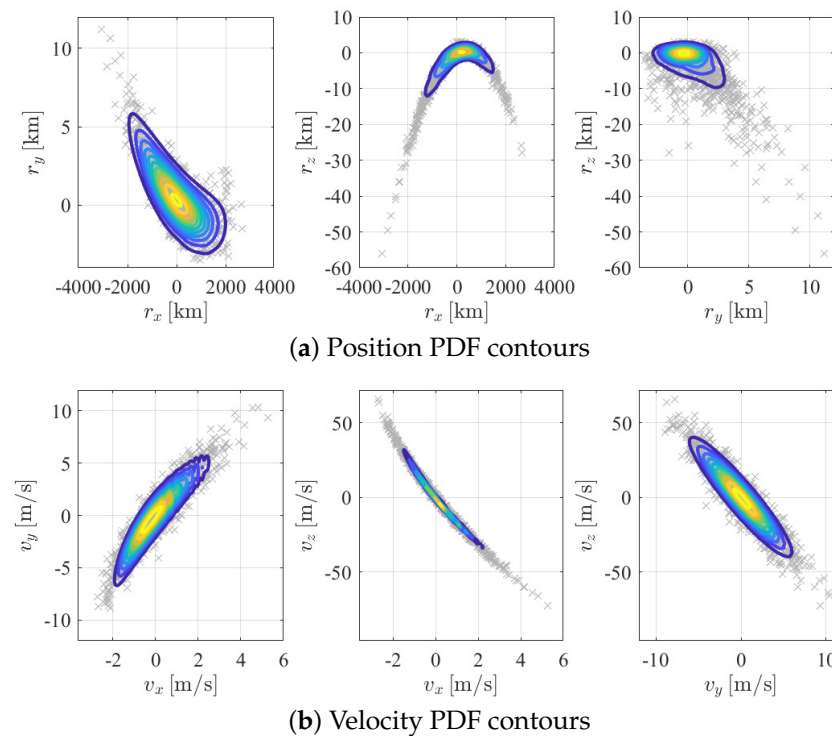


Figure 10. PDF contours using AGMM-VSG with Monte Carlo samples for TQO case.

5. Conclusions

In this paper, to reduce the computational burden while maintaining prediction accuracy in orbital uncertainty propagation, an adaptive Gaussian mixture model using virtual sample generation—noted as AGMM-VSG—is proposed. The splitting algorithm is applied to the dominant eigenvalue of the covariance matrix of the Gaussian components. An active sampling-based KRG algorithm is employed for generating virtual samples, and then propagations are executed based on these expense-less virtual samples.

The performance of the active sampling-based KRG algorithm is validated using an LEO case considering the atmospheric drag. Numerical simulation shows that the proposed active sampling-based KRG algorithm can accurately approximate the orbit state using only 10 samples.

Moreover, the proposed AGMM-VSG is successfully applied to solve the orbit uncertainty propagation problem in LEO, HEO, and Tianqin orbit cases. It was demonstrated that the obtained PDF contours using AGMM-VSG are more representative of the curvature of the true distribution than the fifth-order CR method. Moreover, likelihood agreement measure tests indicate that the new approach shows close performance in approximating the propagation of uncertainty with the AGMM method, while only 100 evaluations are required. The computational cost of the proposed AGMM-VSG method is only 1/20 that of the conventional GMM method. All in all, the newly presented approach has advantages in accuracy and efficiency over competitive methods.

Author Contributions: Conceptualization, T.X. and Z.Z.; methodology and software, H.H. All authors have read and agreed to the published version of the manuscript.

Funding: This research was funded by the National Natural Science Foundation of China (Grant No. U20B2001), the National Key R&D Program of China (Grant No. 2020YFC2201200) and the Basic Scientific Research Project (Grant No. JCKY2020903B002).

Institutional Review Board Statement: Not applicable.

Informed Consent Statement: Not applicable.

Data Availability Statement: Not applicable.

Conflicts of Interest: The authors declare no conflict of interest.

References

1. Wen, C.; Peng, C.; Gao, Y. Reachable domain for spacecraft with ellipsoidal Delta-V distribution. *Astrodynamics* **2018**, *2*, 265–288. [\[CrossRef\]](#)
2. Qiao, D.; Zhou, X.; Li, X. Analytical configuration uncertainty propagation of geocentric interferometric detection constellation. *Astrodynamics* **2023**. [\[CrossRef\]](#)
3. Oguri, K.; McMahon, J.W. Stochastic primer vector for robust low-thrust trajectory design under uncertainty. *J. Guid. Control Dyn.* **2022**, *45*, 84–102. [\[CrossRef\]](#)
4. Shu, P.; Yang, Z.; Luo, Y.Z. Higher-Order Lambert Problem Solution Based on Differential Algebra. *J. Guid. Control Dyn.* **2022**, *45*, 1913–1926. [\[CrossRef\]](#)
5. Folkner, W.; Hechler, F.; Sweetser, T.; Vincent, M.; Bender, P. LISA orbit selection and stability. *Class. Quantum Gravity* **1997**, *14*, 1405. [\[CrossRef\]](#)
6. Tan, Z.; Ye, B.; Zhang, X. Impact of orbital orientations and radii on TianQin constellation stability. *Int. J. Mod. Phys. D* **2020**, *29*, 2050056. [\[CrossRef\]](#)
7. Zhou, X.; Qin, T.; Meng, L. Maneuvering Spacecraft Orbit Determination Using Polynomial Representation. *Aerospace* **2022**, *9*, 257. [\[CrossRef\]](#)
8. Ye, B.B.; Zhang, X.; Zhou, M.Y.; Wang, Y.; Yuan, H.M.; Gu, D.; Ding, Y.; Zhang, J.; Mei, J.; Luo, J. Optimizing orbits for TianQin. *Int. J. Mod. Phys. D* **2019**, *28*, 1950121. [\[CrossRef\]](#)
9. Luo, Y.Z.; Yang, Z. A review of uncertainty propagation in orbital mechanics. *Prog. Aerosp. Sci.* **2017**, *89*, 23–39. [\[CrossRef\]](#)
10. Terejanu, G.; Singla, P.; Singh, T.; Scott, P.D. Uncertainty propagation for nonlinear dynamic systems using Gaussian mixture models. *J. Guid. Control Dyn.* **2008**, *31*, 1623–1633. [\[CrossRef\]](#)
11. Han, H.; Qiao, D.; Chen, H.; Li, X. Rapid planning for aerocapture trajectory via convex optimization. *Aerosp. Sci. Technol.* **2019**, *84*, 763–775. [\[CrossRef\]](#)
12. Fuller, A. Analysis of nonlinear stochastic systems by means of the Fokker–Planck equation. *Int. J. Control.* **1969**, *9*, 603–655. [\[CrossRef\]](#)
13. Chen, N.; Majda, A.J.; Tong, X.T. Rigorous Analysis for Efficient Statistically Accurate Algorithms for Solving Fokker–Planck Equations in Large Dimensions. *SIAM/ASA J. Uncertain. Quantif.* **2018**, *6*, 1198–1223. [\[CrossRef\]](#)
14. Junkins, J.L.; Akella, M.R.; Alfrined, K.T. Non-Gaussian error propagation in orbital mechanics. *Guid. Control.* **1996**, *1996*, 283–298.
15. Ghoreishi, S.; Allaire, D. Adaptive uncertainty propagation for coupled multidisciplinary systems. *AIAA J.* **2017**, *55*, 3940–3950. [\[CrossRef\]](#)
16. Jia, B.; Xin, M. Active Sampling Based Polynomial-Chaos-Kriging Model for Orbital Uncertainty Propagation. *J. Guid. Control Dyn.* **2021**, *44*, 905–922. [\[CrossRef\]](#)
17. Park, R.S.; Scheeres, D.J. Nonlinear mapping of Gaussian statistics: theory and applications to spacecraft trajectory design. *J. Guid. Control Dyn.* **2006**, *29*, 1367–1375. [\[CrossRef\]](#)
18. Chen, Q.; Qiao, D.; Wen, C. Reachable domain of spacecraft after a gravity-assist flyby. *J. Guid. Control Dyn.* **2019**, *42*, 931–940. [\[CrossRef\]](#)

19. Chen, Q.; Qiao, D.; Wen, C. Orbital Element Reachable Set After Gravity Assists of Planets in Elliptical Orbits. *J. Guid. Control Dyn.* **2020**, *43*, 989–997. [\[CrossRef\]](#)
20. Yang, Z.; Luo, Y.Z.; Zhang, J. Nonlinear semi-analytical uncertainty propagation of trajectory under impulsive maneuvers. *Astrodynamics* **2019**, *3*, 61–77. [\[CrossRef\]](#)
21. Shu, P.; Yang, Z.; Luo, Y.Z.; Sun, Z.J. Collision Probability of Debris Clouds Based on Higher-Order Boundary Value Problems. *J. Guid. Control Dyn.* **2022**, *45*, 1512–1522. [\[CrossRef\]](#)
22. Park, R.S.; Scheeres, D.J. Nonlinear semi-analytic methods for trajectory estimation. *J. Guid. Control Dyn.* **2007**, *30*, 1668–1676. [\[CrossRef\]](#)
23. Majji, M.; Junkins, J.L.; Turner, J.D. A high order method for estimation of dynamic systems. *J. Astronaut. Sci.* **2008**, *56*, 401–440. [\[CrossRef\]](#)
24. Zhou, X.; Qin, T.; Ji, M.; Qiao, D. A LSTM assisted orbit determination algorithm for spacecraft executing continuous maneuver. *Acta Astronaut.* **2022**. [\[CrossRef\]](#)
25. Boone, S.; McMahon, J. Orbital guidance using higher-order state transition tensors. *J. Guid. Control Dyn.* **2021**, *44*, 493–504. [\[CrossRef\]](#)
26. Qiao, D.; Zhou, X.; Zhao, Z.; Qin, T. Asteroid Approaching Orbit Optimization Considering Optical Navigation Observability. *IEEE Trans. Aerosp. Electron. Syst.* **2022**, *58*, 5165–5179. [\[CrossRef\]](#)
27. Wang, Z.; Wang, X.; Liang, Y.; Yang, F. A new sigma-point filter–uniform random sampling Kalman filter. *IFAC-PapersOnLine* **2017**, *50*, 3853–3858. [\[CrossRef\]](#)
28. Li, X.; Qiao, D.; Li, P. Bounded trajectory design and self-adaptive maintenance control near non-synchronized binary systems comprised of small irregular bodies. *Acta Astronaut.* **2018**, *152*, 768–781. [\[CrossRef\]](#)
29. Han, H.; Qiao, D.; Chen, H. Optimization of aeroassisted rendezvous and interception trajectories between non-coplanar elliptical orbits. *Acta Astronaut.* **2019**, *163*, 190–200. [\[CrossRef\]](#)
30. Jia, B.; Xin, M. Short-arc orbital uncertainty propagation with arbitrary polynomial chaos and admissible region. *J. Guid. Control Dyn.* **2020**, *43*, 715–728. [\[CrossRef\]](#)
31. Julier, S.J.; Uhlmann, J.K.; Durrant-Whyte, H.F. A new approach for filtering nonlinear systems. In Proceedings of the American Control Conference-ACC'95, Seattle, WA, USA, 21–23 June 1995; Volume 3, pp. 1628–1632.
32. Van Der Merwe, R. *Sigma-point Kalman Filters for Probabilistic Inference in Dynamic State-Space Models*; Oregon Health & Science University: Portland, OR, USA, 2004.
33. Meng, D.; Miao, L.; Shao, H.; Shen, J. A seventh-degree cubature Kalman filter. *Asian J. Control.* **2018**, *20*, 250–262. [\[CrossRef\]](#)
34. Cui, X.; Jing, Z.; Luo, M.; Guo, Y.; Qiao, H. A new method for state of charge estimation of lithium-ion batteries using square root cubature Kalman filter. *Energies* **2018**, *11*, 209. [\[CrossRef\]](#)
35. Zhang, X.; Yan, Z.; Chen, Y. High-degree cubature Kalman filter for nonlinear state estimation with missing measurements. *Asian J. Control.* **2022**, *24*, 1261–1272. [\[CrossRef\]](#)
36. Chen, P.; Zabararas, N.; Bilionis, I. Uncertainty propagation using infinite mixture of gaussian processes and variational bayesian inference. *J. Comput. Phys.* **2015**, *284*, 291–333. [\[CrossRef\]](#)
37. Li, X.; Warier, R.R.; Sanyal, A.K.; Qiao, D. Trajectory tracking near small bodies using only attitude control. *J. Guid. Control Dyn.* **2019**, *42*, 109–122. [\[CrossRef\]](#)
38. Jones, B.A.; Weisman, R. Multi-fidelity orbit uncertainty propagation. *Acta Astronaut.* **2019**, *155*, 406–417. [\[CrossRef\]](#)
39. Sun, P.; Colombo, C.; Trisolini, M.; Li, S. Hybrid Gaussian Mixture Splitting Techniques for Uncertainty Propagation in Nonlinear Dynamics. *J. Guid. Control Dyn.* **2022**, 1–11. [\[CrossRef\]](#)
40. Vittaldev, V.; Russell, R.P.; Linares, R. Spacecraft uncertainty propagation using gaussian mixture models and polynomial chaos expansions. *J. Guid. Control Dyn.* **2016**, *39*, 2615–2626. [\[CrossRef\]](#)
41. Vittaldev, V.; Russell, R.P. Space object collision probability using multidirectional gaussian mixture models. *J. Guid. Control Dyn.* **2016**, *39*, 2163–2169. [\[CrossRef\]](#)
42. DeMars, K.J.; Bishop, R.H.; Jah, M.K. Entropy-based approach for uncertainty propagation of nonlinear dynamical systems. *J. Guid. Control Dyn.* **2013**, *36*, 1047–1057. [\[CrossRef\]](#)
43. Zhou, X.; Cheng, Y.; Qiao, D.; Huo, Z. An adaptive surrogate model-based fast planning for swarm safe migration along halo orbit. *Acta Astronaut.* **2022**, *194*, 309–322. [\[CrossRef\]](#)
44. Zhou, X.; Wang, S.; Qin, T. Multi-Spacecraft Tracking and Data Association Based on Uncertainty Propagation. *Appl. Sci.* **2022**, *12*, 7660. [\[CrossRef\]](#)
45. Tang, Y.; Long, T.; Shi, R.; Wu, Y.; Gary Wang, G. Sequential radial basis function-based optimization method using virtual sample generation. *J. Mech. Des.* **2020**, *142*, 111701. [\[CrossRef\]](#)
46. Shi, R.; Long, T.; Baoyin, H. Multi-fidelity and multi-objective optimization of low-thrust transfers with control strategy for all-electric geostationary satellites. *Acta Astronaut.* **2020**, *177*, 577–587. [\[CrossRef\]](#)
47. Zhao-Ming, L.; Wen-Ge, Y.; Dan, D.; Yu-Rong, L. A novel algorithm of fifth-degree cubature Kalman filter for orbit determination at the lower bound approaching to the number of cubature points. *Acta Phys. Sin.* **2017**, *66*. [\[CrossRef\]](#)
48. Vishwajeet, K.; Singla, P. Adaptive split/merge-based Gaussian mixture model approach for uncertainty propagation. *J. Guid. Control Dyn.* **2018**, *41*, 603–617. [\[CrossRef\]](#)

49. Omran, A.; Newman, B. Nonlinearity Index Theory for Flight Mechanics Applications. In Proceedings of the AIAA Atmospheric Flight Mechanics Conference, Toronto, ON, Canada, 2–5 August 2010; p. 7624.
50. Manchester, Z.; Kuindersma, S. Derivative-free trajectory optimization with unscented dynamic programming. In Proceedings of the IEEE 55th Conference on Decision and Control (CDC), Las Vegas, NV, USA, 12–14 December 2016; pp. 3642–3647.
51. Bouhlel, M.A.; Martins, J.R. Gradient-enhanced kriging for high-dimensional problems. *Eng. Comput.* **2019**, *35*, 157–173. [[CrossRef](#)]
52. Gao, A.; Liao, W. Efficient gravity field modeling method for small bodies based on Gaussian process regression. *Acta Astronaut.* **2019**, *157*, 73–91. [[CrossRef](#)]
53. Sun, F.; Su, W.Y.; Wang, M.Y.; Wang, R.J. RBF-POD reduced-order modeling of flow field in the curved shock compression inlet. *Acta Astronaut.* **2021**, *185*, 25–36. [[CrossRef](#)]
54. Jia, F.; Li, X.; Qiao, D.; Zhou, X. Semi-analytical configuration optimization of geocentric gravitational wave observatory. *Acta Astronaut.* **2023**, *202*, 522–534. [[CrossRef](#)]

Disclaimer/Publisher’s Note: The statements, opinions and data contained in all publications are solely those of the individual author(s) and contributor(s) and not of MDPI and/or the editor(s). MDPI and/or the editor(s) disclaim responsibility for any injury to people or property resulting from any ideas, methods, instructions or products referred to in the content.